Supplementary Information

Forming three-dimensional micro-objects using two-dimensional gradient printing

Aofei Mao, Peixun Fan, Loic Constantin, Nan Li, Xi Huang, Bai Cui, Jean-Francois Silvain, Xinwei Wang & Yong Feng Lu**

E-mail: ylu2@unl.edu; fanpeixun@gmail.com.

This Supporting Information document includes:

Mechanisms for 2D-3D Transformation

Supplemental Results & Figures S1 to S19

Supplemental Table

Additional Supplementary Video available online:

Formation of arbitrary objects through 2D printing and 2D-3D transformation.

Table of Contents

List of Acronyms

TPP	two-photon polymerization
fs	femtosecond
2D	two dimensional
3D	three dimensional
2D-3D	2D-to-3D
LP	laser power
SS	scan speed
HD	hatching distance
SD	slicing distance
HA	hatching angle
DoC	degree of conversion
PGMEA	propylene glycol monomethyl ether acetate
SEM	scanning electron microscope

1. Mechanisms for 2D-3D Transformation

1.1 Conceptualization of 2D-3D transformation

Figure S1 schematically illustrates the concept to flexibly construct three-dimensional (3D) micro-objects via two-dimensional (2D) printing. The femtosecond (fs) laser two-photon polymerization (TPP) process is used for printing 2D layered patterns unfolded from targeted 3D objects. To enable the spontaneous structural transformation of the 2D patterns after printing, stress profiles are built in the 2D patterns by introducing gradient polymerization (**Figure S1**a). Samples fabricated using TPP tend to shrink after development and drying. By introducing gradient polymerization, the level of shrinkage will be different and location specific in the TPP structures. The non-uniform shrinkage will result in stress. Therefore, through engineering the gradient polymerization, the stress field within the 2D patterns can be tailored. When the stress is released during drying, the 2D patterns are spontaneously transformed to form desired 3D structures, as indicated by the evolution shown in **Figure S1**a to S1d.

The TPP-enabled 2D-to-3D (2D-3D) transformation was developed based on the close "laser dose-degree of conversion (DoC)-shrinkage-stress" relationships. First, the DoC reached in TPP printing depends on the laser doses applied. A higher laser dose generates more radicals, leading to the consumption of more monomers and thus a higher cross-link density, whereas a lower dose results in a lower cross-link density, as illustrated in **Figure S1**b. Thus, the distribution of DoC within the TPP structures can be programmed by controlling the laser doses. Second, the shrinkage level is determined by DoC. The positions with lower cross-link densities tend to shrink more than those with higher cross-link densities when drying up, as shown in **Figure S1**c. Next, the stress originates from the shrinkage difference between adjacent portions of the TPP samples, particularly adjacent printed layers. By specifically controlling the DoC distributions and the consequent shrinkage differences, stress fields can be established in a well-controlled manner. This implies that the 2D-3D structural transformation can also be flexibly manipulated. As an evidence, **Figure S1**e shows a vivid 3D flower-bud structure which was initially written in the polymer resin in a 2D blooming flower pattern (**Figure S1**a) and then spontaneously formed through such a stress-driven transformation process.

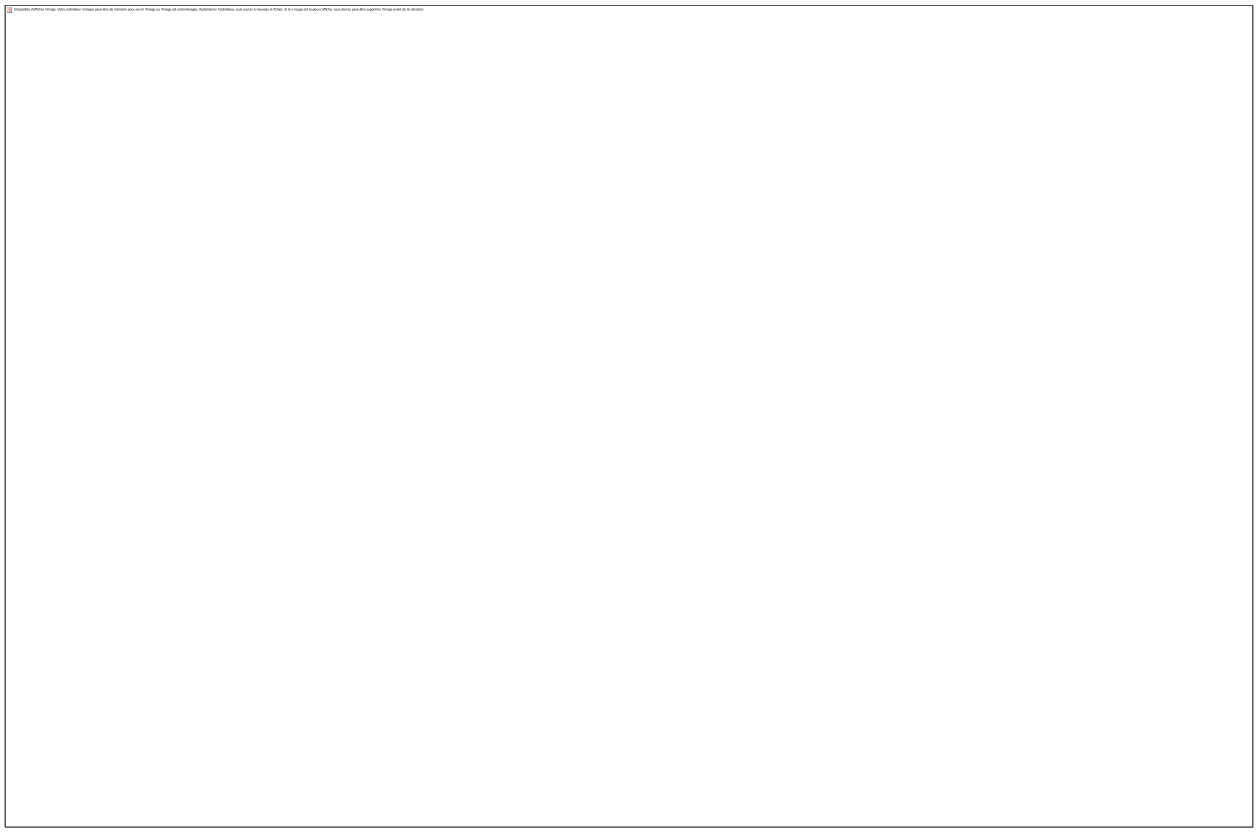

Figure S1. Schematics of the spontaneous 2D-3D structural transformation enabled by spatially controlled polymerization. a) Radial and vertical profiles of polymerization (referred by varied colors) introduced by an fs laser in a 2D pattern of a blooming flower. **b**) Locally programmed DoC by flexibly controlling the laser doses applied. **c**) Local gradients of polymer shrinkage and the resulting stress as a driving force for structural transformation. **d**) The spontaneous 2D-3D transformation process from a 2D blooming flower to a 3D flower bud when dried up. **e**) SEM image of the 3D flower-bud structure formed through 2D-3D transformation. The inset is an optical microscopy image of a 2D blooming flower without DoC gradient for comparison.

1.2 Laser-engineered gradient polymerization and controlled shrinkage

With the TPP-enabled 2D-3D transformation developed, the "laser dose-DoC-shrinkage-stress" relationships were systematically investigated. After TPP printing, the samples were immersed first in propylene glycol monomethyl ether acetate (PGMEA) for 1 h and then in 2-propanol for 20 min, where the unreacted monomers were replaced by PGMEA and then by 2-propanol. During the drying process, the 2-propanol evaporates, making the polymer networks loosely supported and shrink in accordance with the DoC. As illustrated in **Figure S2**a, the shrinkage is negatively related to the DoC while the DoC is positively related to the laser dose. When printed

with a higher laser dose, more monomers will be consumed, leading to polymer networks with a higher DoC/cross-link density which has a weaker tendency to shrink and vice versa.[1]

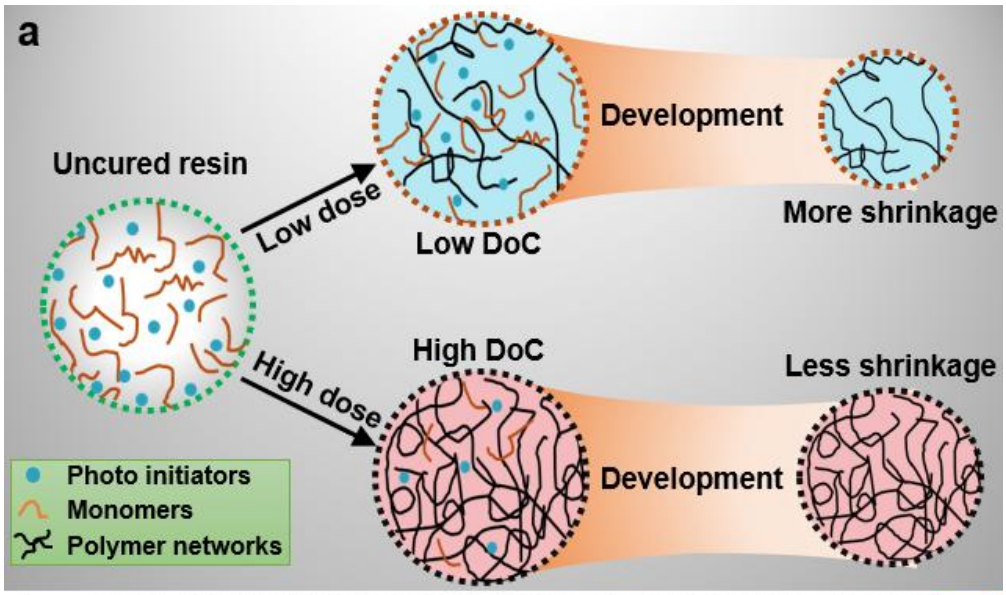

c

Specific Parameters Used				
DoC	LP	SS	HD	SD
Low	19.25 mW		0.35 μm	0.6 μm
Medium	22 mW	10 mm/s	0.2 μm	0.2 μm
High	24.75 mW		0.2 μm	0.2 μm

Figure S2. Laser-dose defined DoC and shrinkage. a) Schematic of the "laser dose-DoC-shrinkage" relationships. **b**) Verification of the dependence of the DoC and shrinkage on the laser doses using confocal fluorescence microscopy. "Low", "Medium", and "High" refer to laser doses and DoCs in the SEM and fluorescence images, respectively. **c**) Specific parameters used for printing the samples in b).

To verify the dependence of the DoC and shrinkage on the laser doses, four polymer cubes were printed with different sets of printing parameters (as summarized in **Figure S2**c) using the same CAD model. The SEM images in **Figure S2**b confirm that the cube printed with a low laser dose shrinks most. Meanwhile, the cubes printed with high, medium, and low laser doses show high, medium, and low fluorescence intensities, respectively. It is known that the fluorescence intensity is proportional to the concentration of polymer networks.[2] A higher fluorescence intensity indicates a higher cross-link density, namely, a higher DoC. Therefore, the positive dependence of DoC and negative dependence of shrinkage on the laser dose are evidenced. Both the DoC distribution and shrinkage difference within 2D layered patterns and, thus, the stress fields yielded, can be controlled by adjusting the TPP printing parameters.

Attributing to the nonlinear two-photon absorption process, the TPP only occurs within a nanoscale elliptical voxel around the fs laser focal spot. Through overlapping voxels in a line-by-line and layer-by-layer fashion, an area or volume can be covered by TPP. The fs laser used in this research works at a repetition rate of 80 MHz and has a focal spot of ~2.7 μm^2 under the 63× objective lens based on our calculation. Briefly, the laser doses can be controlled in two ways, as illustrated in **Figure S3**.

- The first way is to control the voxel/line size by tuning the laser power (LP) and the voxel overlap within each line by tuning the scan speed (SS). Tuning both the LP and SS determines the DoC distribution within each TPP line, through which the axial and radial shrinkage of the TPP lines can be tailored.
- The second way is to control the voxel distribution and overlap by changing the hatching distance (HD) and slicing distance (SD). The voxels have an aspect ratio (depth/width) of ~2.6 using the 63× lens and the IP-Dip resin, while the corresponding voxel width varies in a range of 300-900 nm depending on the printing parameters.[3,4] By separately or synchronously changing the HD and SD between 100-900 and 200-2340 nm, respectively, the overlapping ratio between the adjacent lines/layers can be easily tuned.

These tunable parameters (LP, SS, HD, and SD) make the TPP-enabled 2D-3D transformation programmable in fabricating various 3D micro-objects.

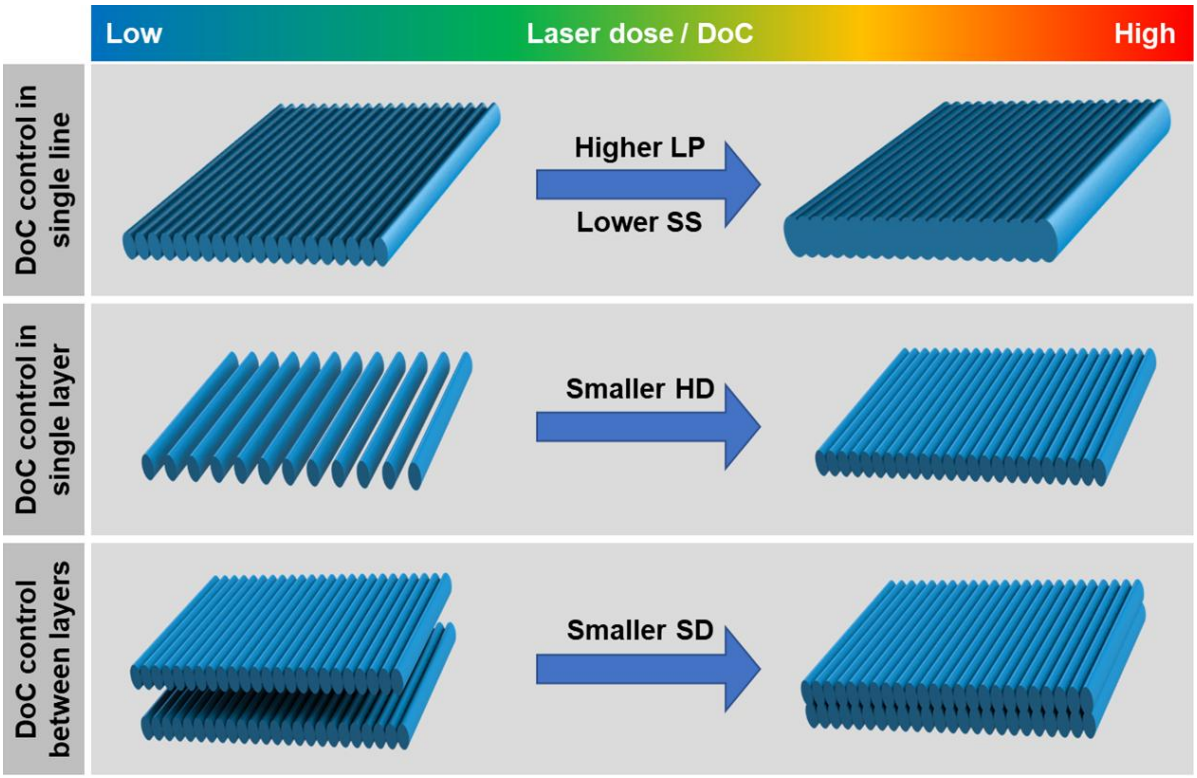

Figure S3. Schematics for tailoring DoC through controlling laser doses in TPP printing.

In addition to the simple flower-bud structure demonstrated in **Figure S1**, we also succeeded in fabricating an entire free-standing flower composed of multiple features (e.g., three layers of petals, four stamens, and one pedicle) through the 2D-3D transformation, as shown in **Figure S4**. All the petals and stamens were printed in either horizontal or vertical planes, as shown in the inset of **Figure S4**b. By adjusting the printing parameters and introducing different gradient profiles of DoC at different portions of the flower, stress fields of different levels in different directions were established in the flower. As the stress was released, the petals, stamens, and pedicle simultaneously performed different types of structural transformations (e.g., bending and spiraling), producing the sophisticated 3D standing flower. **Figure S4**a shows that an array of the free-standing flower were identically fabricated in one batch, confirming the reproducibility of the 2D-3D transformation approach.

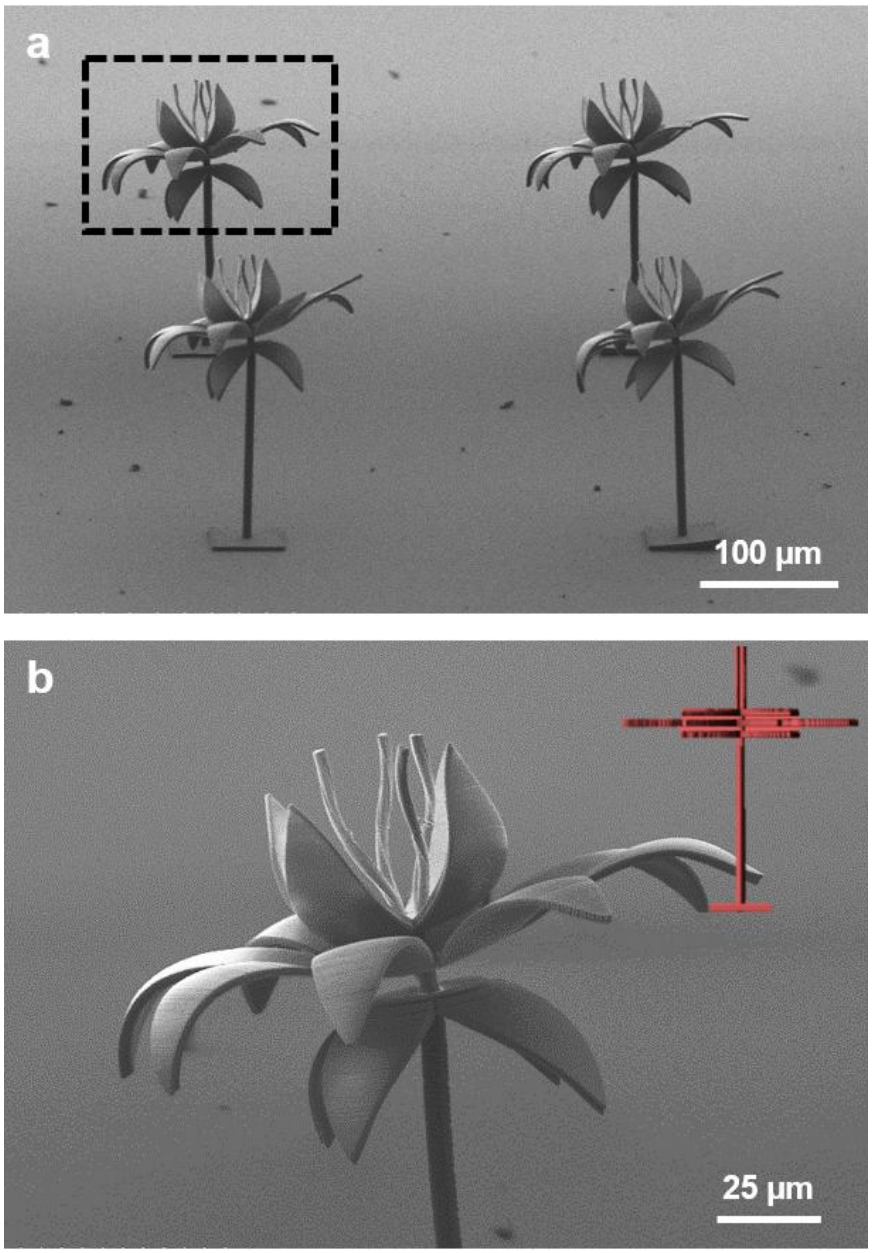

Figure S4. An array of identical entire standing-flower structures fabricated via the 2D-3D transformation. a) SEM image of the array. **b**) Zoomed-in SEM image for the dashed area in (**a**) showing the details of a flower. The inset of **b** is the front-view design of the entire standing flower, showing that all portions of the flower were printed in either horizontal or vertical 2D planes. As can be seen, the head part of the pedicle bent to the left together with the stamens and petals after the 2D-3D transformation. Meanwhile, the stamens twisted and the petals bent either upwards or downwards.

2. Supplemental Results & Figures

2.1 Systematic investigations of polymer shrinkage behaviors

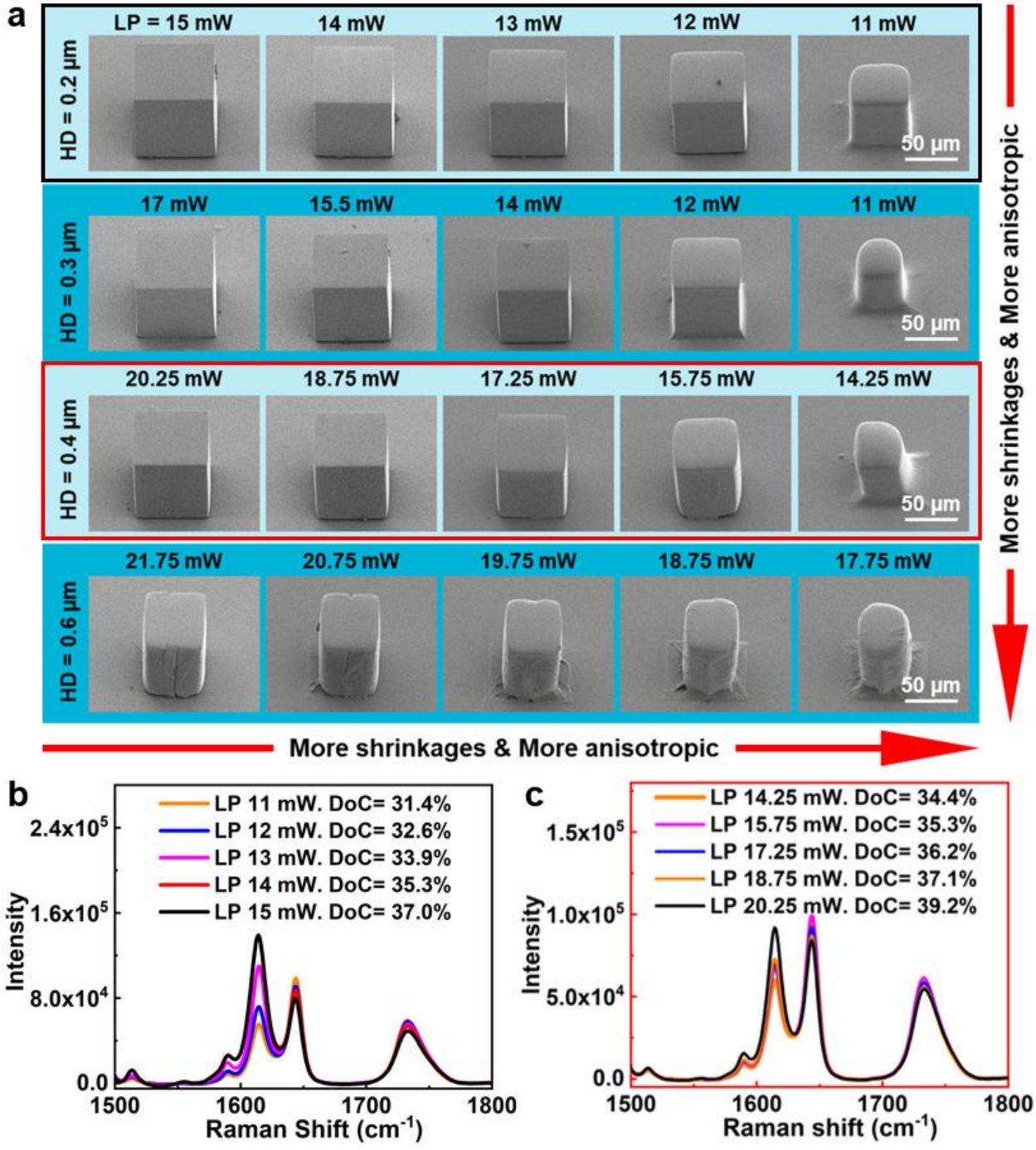

Figure S5. Representative SEM images and Raman spectra from our systematic investigation. a) Both LP and HD were shown for each SEM image while the other parameters were kept constant (SD/HD = 2, SS = 10 mm/s). For all samples, laser hatching was conducted vertically. **b**) and **c**) The Raman spectra for samples marked in black and red boxes in **a**), respectively. The calculated DoCs were also shown for comparison.

To achieve controllable 2D-3D structural transformation and guide the selection of printing parameters, we systematically investigated the influence of major printing parameters (LP, SS, HD, and SD) on the shrinkage behaviors. Around 100 cubic blocks (50×50×50 μm^3) were printed using the same CAD model with varying parameters as listed in the **Supplemental Table**. As shown by the representative SEM images in **Figure S5**a, both the shrinkage levels and isotropy/anisotropy can be well controlled by adjusting the TPP printing conditions. Also, we characterized all the cubic blocks using Raman spectroscopy to study the "laser dose-DoC-shrinkage" relationships, with the representative Raman spectra shown in **Figure S5**b,c. When other printing parameter are fixed (e.g., at a fixed HD of 0.2 or 0.4 μm), a lower laser dose (e.g., a lower laser power) results in a higher shrinkage and a lower DoC. Therefore, shrinkage is negatively correlated to the DoC. Hence, the DoC can be used as an indicator of shrinkage levels.

"During the calculation of the DoCs, to take into account the influence of the surrounding peaks in the Raman spectra due to peak overlapping (**Figure S6**a), we first fit the raw Raman spectra using the Lorentz function. After fitting, four separate peaks (i.e., the red, green, blue, and cyan peaks in **Figure S6**b) can be clearly seen. We then measured the integrated intensities of the fitted C=C and C=O peaks (rather than the C=C and C=O peaks in the raw spectra) for calculating DoCs, as indicated by the shadowed blue and cyan areas in **Figure S6**b."

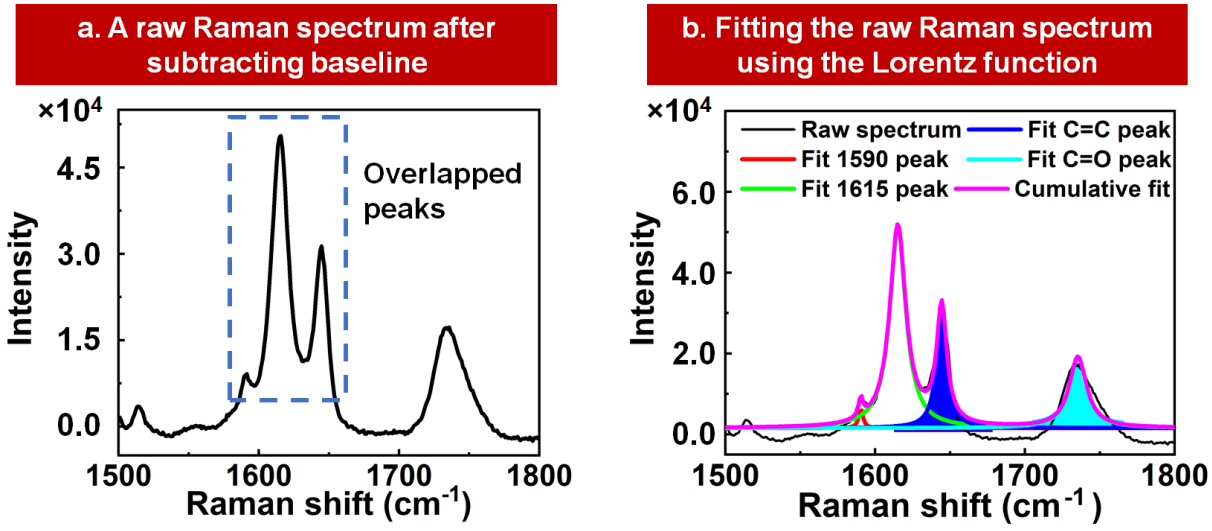

Figure S6. Multiple-peak fitting of the Raman spectra for calculating DoCs. **a**) A typical raw Raman spectrum showing the overlapping of the adjacent peaks. **b**) Multiple-peak fitting of the raw Raman spectrum to obtain separate peaks using the Lorentz function.

To more clearly show the relationships between the laser dose, DoC, and shrinkage, a series

of measured DoC and volume shrinkages for cubic blocks were compiled and shown in **Figure S7**. A negative correlation can be found between the shrinkage and laser dose, while a positive correlation can be found between the DoC with the lase dose. Understanding the "laser dose-DoC-shrinkage" relationships enabled the selection of proper parameter windows for introducing adequate DoC gradients to realize various structural transformations.

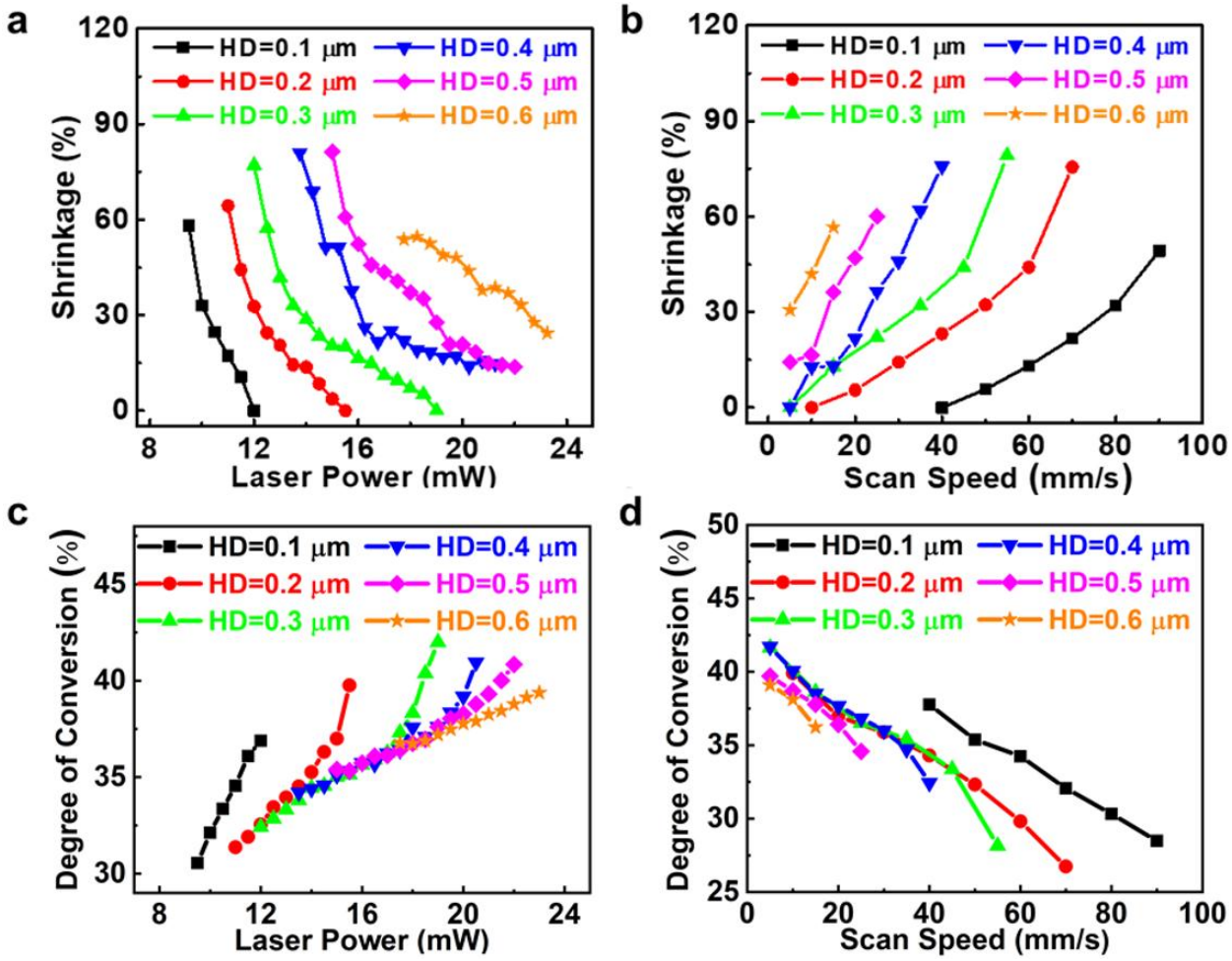

Figure S7. The measured volume shrinkages and DoC for cubic blocks printed using the parameters listed in the Supplemental Table. A fixed scan speed of 10 mm/s was used in **a**, **c**. A fixed laser power of 20 W was used in **b**, **d**.

2.2 Anisotropic shrinkage and directional bending associated with the hatching direction

To realize 2D-3D structural transformation, anisotropic shrinkages are preferred. **Figure S5** has shown that the shrinkage can be controlled either isotropically or anisotropically by adjusting the TPP printing conditions. **Figure S8** further shows that HD is a key factor to determine the

shrinkage isotropy/anisotropy. When a small HD (e.g., 0.3 and 0.1 μm) is used, the cubic blocks show similar shrinkages in both directions parallel and perpendicular to the hatching lines. In contrast, when a large HD (e.g., 0.5 μm) is used, the cubic blocks exhibit obviously more shrinkages perpendicular to the hatching lines.

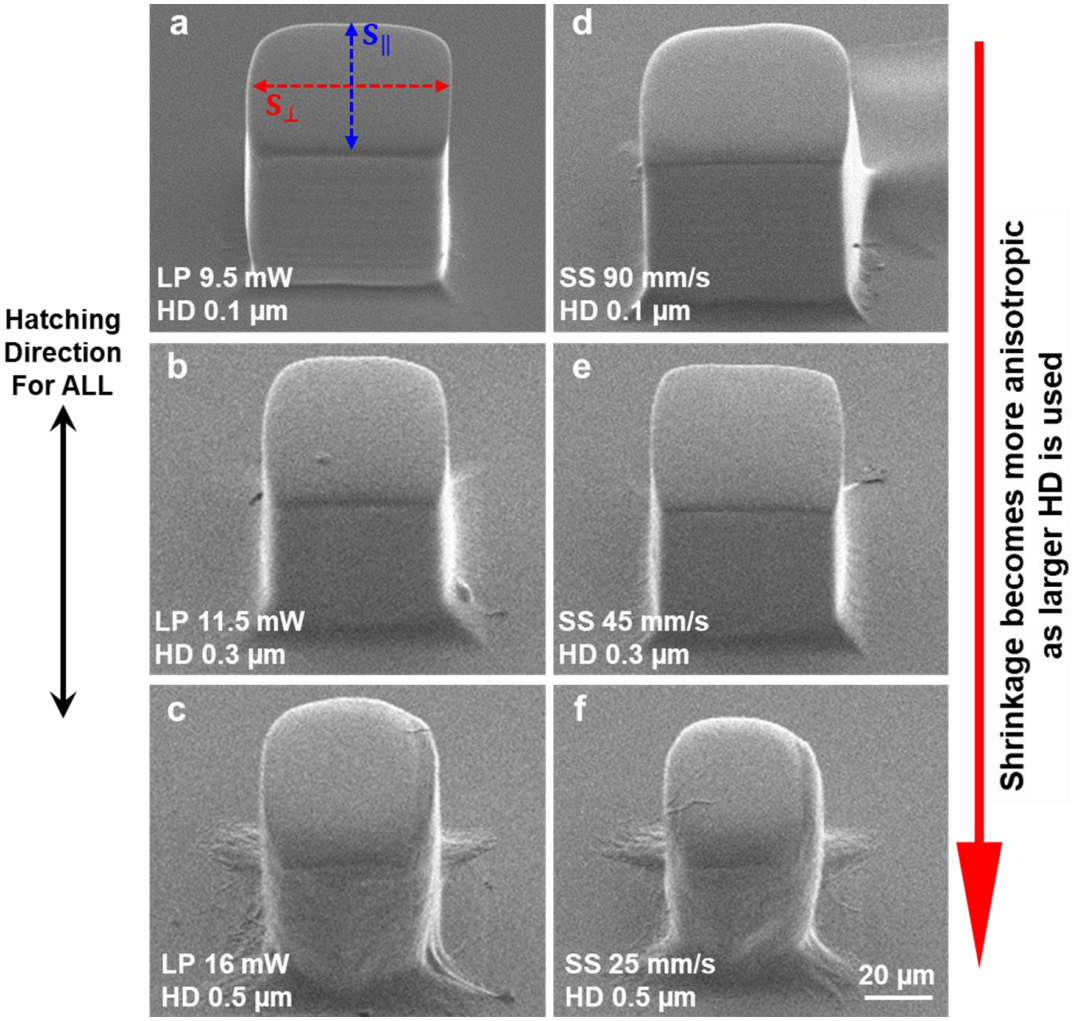

Figure S8. SEM images for a series of cubic blocks with maximum measurable shrinkages at different HDs. The blocks cannot survive the development any more when lower laser doses were used to induce more shrinkages. Although all six blocks exhibit significant volume shrinkages, the shrinkage mainly occurs in the direction perpendicular to the hatching lines when a HD of 0.5 μm was used.

To further clarify the conditions for anisotropic shrinkage, the shrinkages of the cubic blocks both parallel and perpendicular to the hatching lines were separately measured, as shown in **Figure S9**. It can be found that the difference between the shrinkages in the two directions increases as larger HDs are used, no matter the controlling parameter is LP or SS. A HD of

0.4 μm is a threshold value to realize obvious anisotropy.

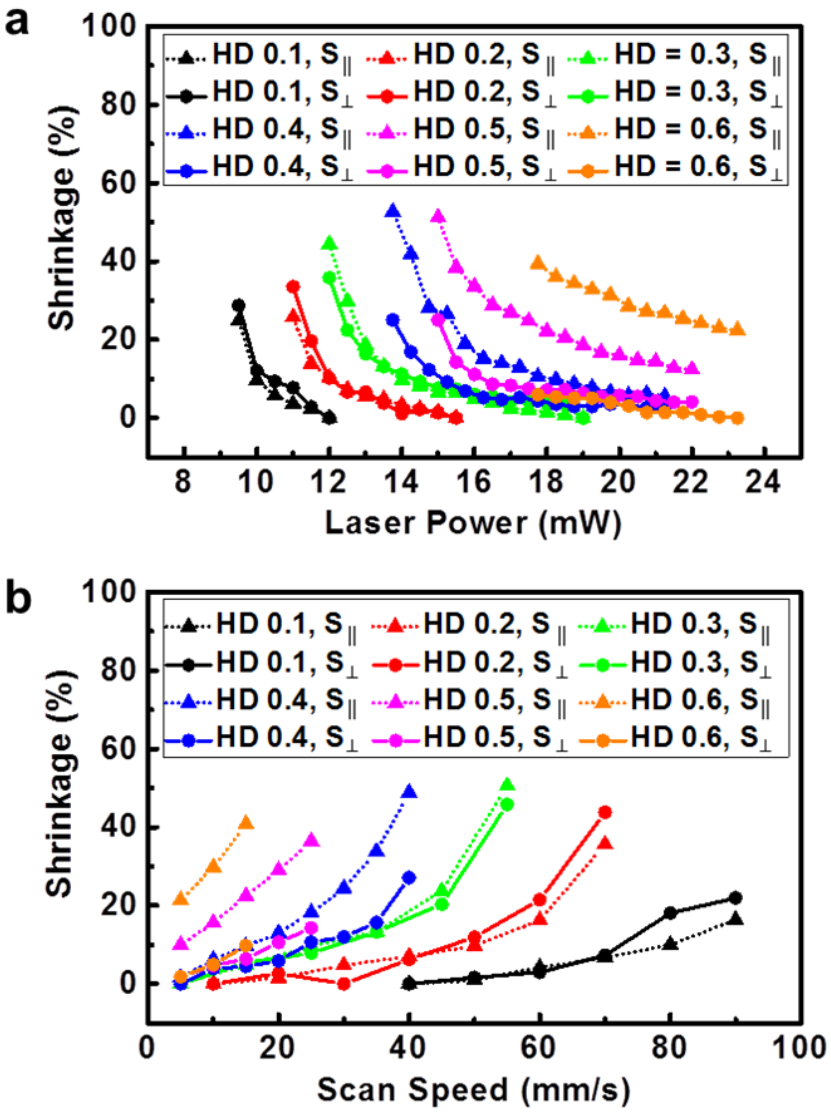

Figure S9. Influence of HD on the shrinkage anisotropy. The anisotropic shrinkages in two directions (i.e., parallel and perpendicular to the hatching direction) manifest at larger HDs. The unit of HD is μm. A fixed scan speed of 10 mm/s was used in **a**. A fixed laser power of 20 W was used in **b**.

The anisotropic shrinkage originates from the Gaussian profile of the fs laser used, where the distribution of photon density follows the Gaussian function,

$$E\,(r,z) = E_0 \frac{\omega_0}{\omega(z)} e^{\frac{-r^2}{w(z)^2}}, \qquad (1)$$

where E_0 is the amplitude of the electric field, r is the radial distance from the central axis of the

beam, z is the axial distance from the focal spot, ω_0 is the waist radius, $\omega(z)$ is the beam radius at plane-z. It is known that the two-photon absorption rate depends on the square of laser intensity. Due to the Gaussian profile of the focused laser spot, the two-photon absorption rate also varies in a Gaussian trend, resulting in a Gaussian distribution of the DoC in the cross-section of each voxel/line, as illustrated in **Figure S10**a, b.

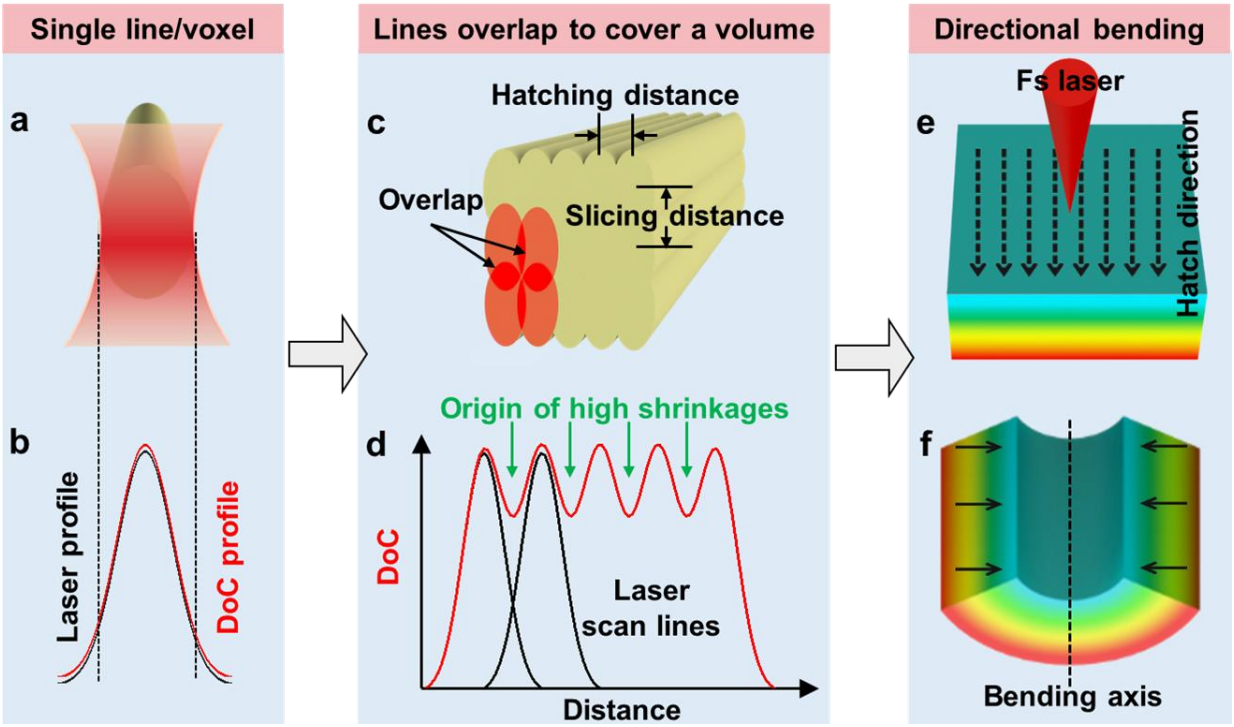

Figure S10. Origin of the anisotropic shrinkage behaviors. a, **b**) Due to the Gaussian profile of the focused laser beam, the voxel lines usually possess gradient DoCs along the radial direction. **c-f**) Provided that the HD is large enough, namely, the line overlap is small enough, the anisotropic DoC distribution remains after the printing, which finally induces anisotropic shrinkage and directional bending in the TPP 2D patterns.

To cover a volume using TPP, overlapping between TPP lines is necessary (**Figure S10**c). When a high overlapping ratio is applied (e.g., using small HDs), the overlap regions can reach a DoC of the same level as in the center of each line, making the whole sample printed homogeneously for isotropic shrinkages. However, when a low overlapping ratio is applied (e.g., using large HDs), the overlap regions can only reach lower DoCs than in the center of each line and act as the origin of high shrinkages (**Figure S10**d). Consequently, the whole printed sample becomes inhomogeneous and tends to shrink more perpendicular to the hatching lines, generating the corresponding stress field for enabling structural transformation (**Figure S10**e, f).

Since bending (or folding) is one most used structural transformation process, we herein take bending as an example to demonstrate how 2D-3D transformation is realized through the anisotropic shrinkage. **Figure S10**e-f demonstrates that the anisotropic shrinkage enables bending perpendicular to the TPP hatching lines. In addition to the basic single-direction bending (namely rolling), we have also achieved wavy bending through alternating the direction of DoC gradients (**Figure S11**a-c**)**. The bending transformation can also be designed to diagonal rather than parallel/perpendicular to the sides of 2D patterns (**Figure S11**d-f**)**. Besides, when more complex hatching paths are used (e.g., using circular hatching to print a rectangular film), even a bending transformation from a planar film to a cap structure can be realized (**Figure S11**g-i).

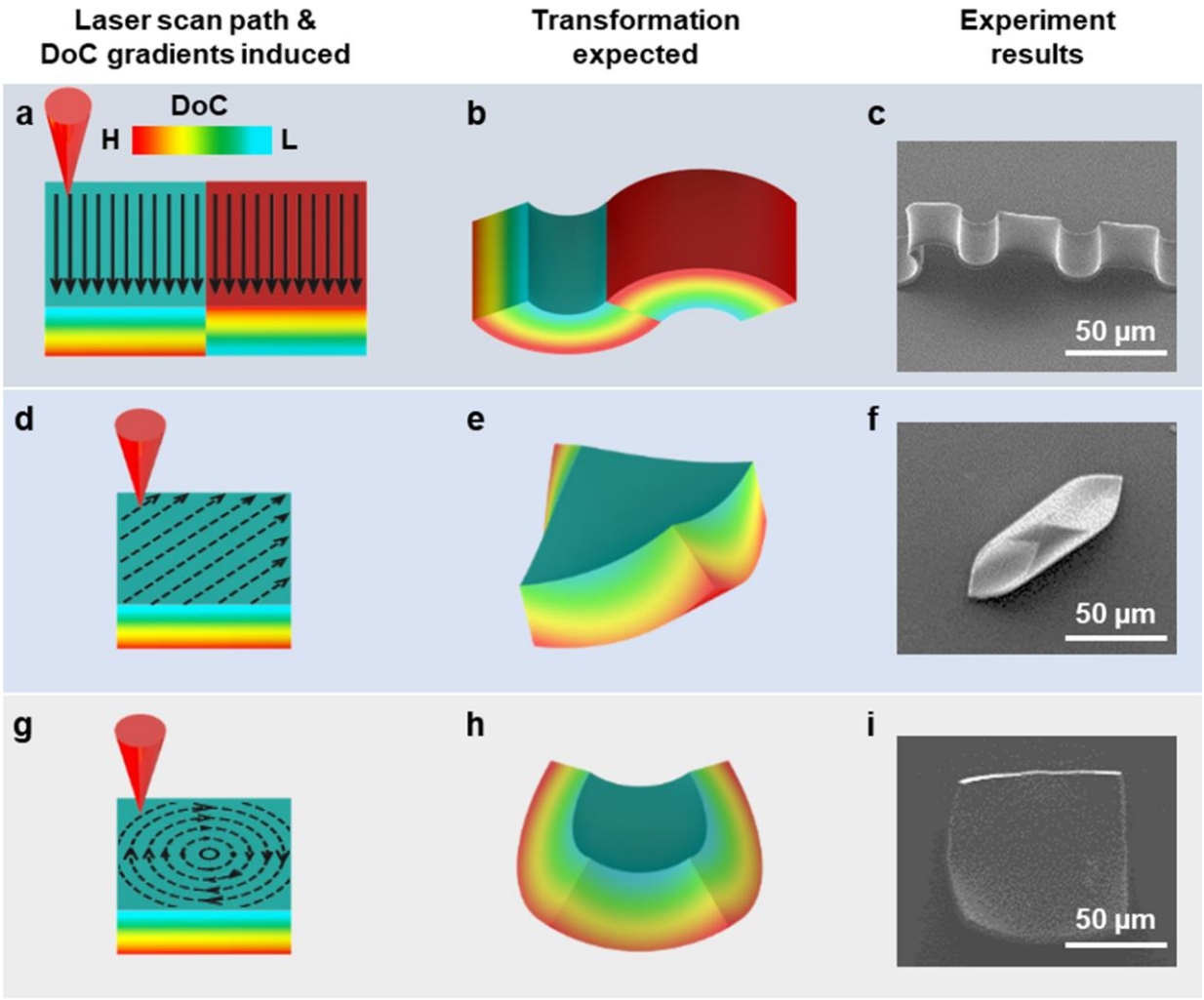

Figure S11. Controlling bending directions by anisotropic shrinkages.

2.3 DoC-gradient defined bending curvature

Since bending can be defined by hatching directions, bending curvatures should also be controllable by tuning the DoC gradients perpendicular to hatching lines. The traditional Timoshenko model was applied here to reach a better control over the bending transformation. To the first approximation, the TPP 2D patterns can be equivalent to a series of local pairs of high- and low-DoC layers, as illustrated in **Figure S12**a. Assuming the shrinkage along the hatching direction is negligible when the shrinkage is mainly controlled perpendicular to the hatching lines, the bending curvature can then be estimated using a classical one-dimensional Timoshenko model:[8]

$$\frac{1}{k} = \frac{24(S_{p,b} - S_{p,t})}{h(14 + n + 1/n)}, \tag{2}$$

where k is the bending curvature, $S_{p,b}/S_{p,t}$ is the shrinkage of the high-/low-DoC layers, h is the overall thickness of the polymer films, and n is the Young's modulus ratio of the low- to the high-DoC layers.

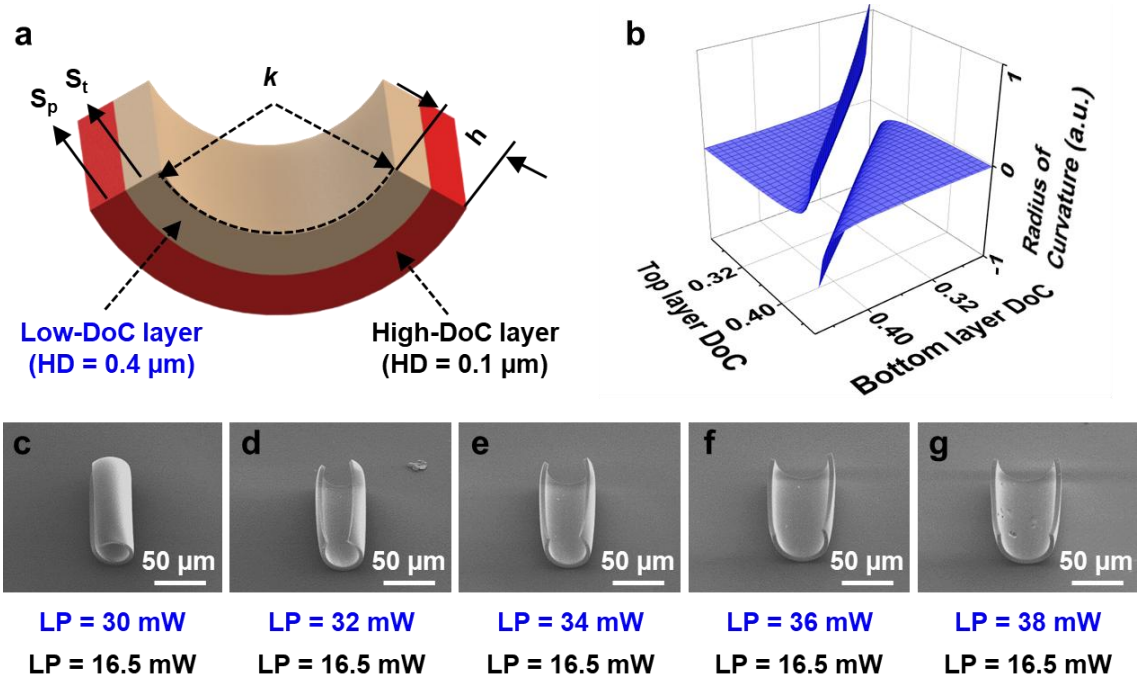

Figure S12. Bending curvatures of TPP films determined by DoC. a) A simplified dual-layer Timoshenko model for analyzing the bending process. **b**) Influence of DoC of the two layers on bending curvatures. **c-g**) SEM images of a series of polymer films printed for testing the model in (**a**). The LP used for printing the high (black) and low (blue) DoC layers of these films are also shown. The SS and SD/HD ratio were fixed at 10 mm/s and two, respectively.

Given that the shrinkages mainly depend on DoC**,** the equation above indicates that the bending curvatures of the polymerized films are determined by the DoC differences in the two layers as long as the film thickness is kept the same, as plotted in **Figure S12**b. Therefore, the local bending and thus the overall 2D-3D transformation of complicated 3D structures can be controlled. **Figure S12**c-g present a series of polymer films in which the bending curvatures are gradually tuned by controlling the DoC differences between the two layers. By simply changing the laser doses (e.g., increasing the LP used for printing the low-DoC layer), the degree of bending transformation can be continuously manipulated, confirming the flexibility of the 2D-3D transformation approach.

2.4 Flexible control of the 2D-3D transformation

Through extending the capability of controlling both the bending direction and curvature, diverse 2D-3D transformations can be further realized, including rolling, coiling, waving, out-of-plane distortion, helical spiraling, *etc*.

Furthermore, by adding particular features on the TPP 2D films, 3D micro-objects having applications in particular fields can be fabricated via the 2D-3D transformation approach. For example, we have achieved a closed 3D microstent transformed from a 2D grid pattern by precisely tuning the DoC gradients normally (**Figure S13**d-f**)**, and a 3D micro-origami structure (a polyhedron with openwork patterns) from a 2D three-pointed-star plate by creating DoC gradients in the hinge regions (**Figure S13**g-h). The 3D microstent and micro-origami structures have potential applications in biomedicine and microelectromechanics, respectively.

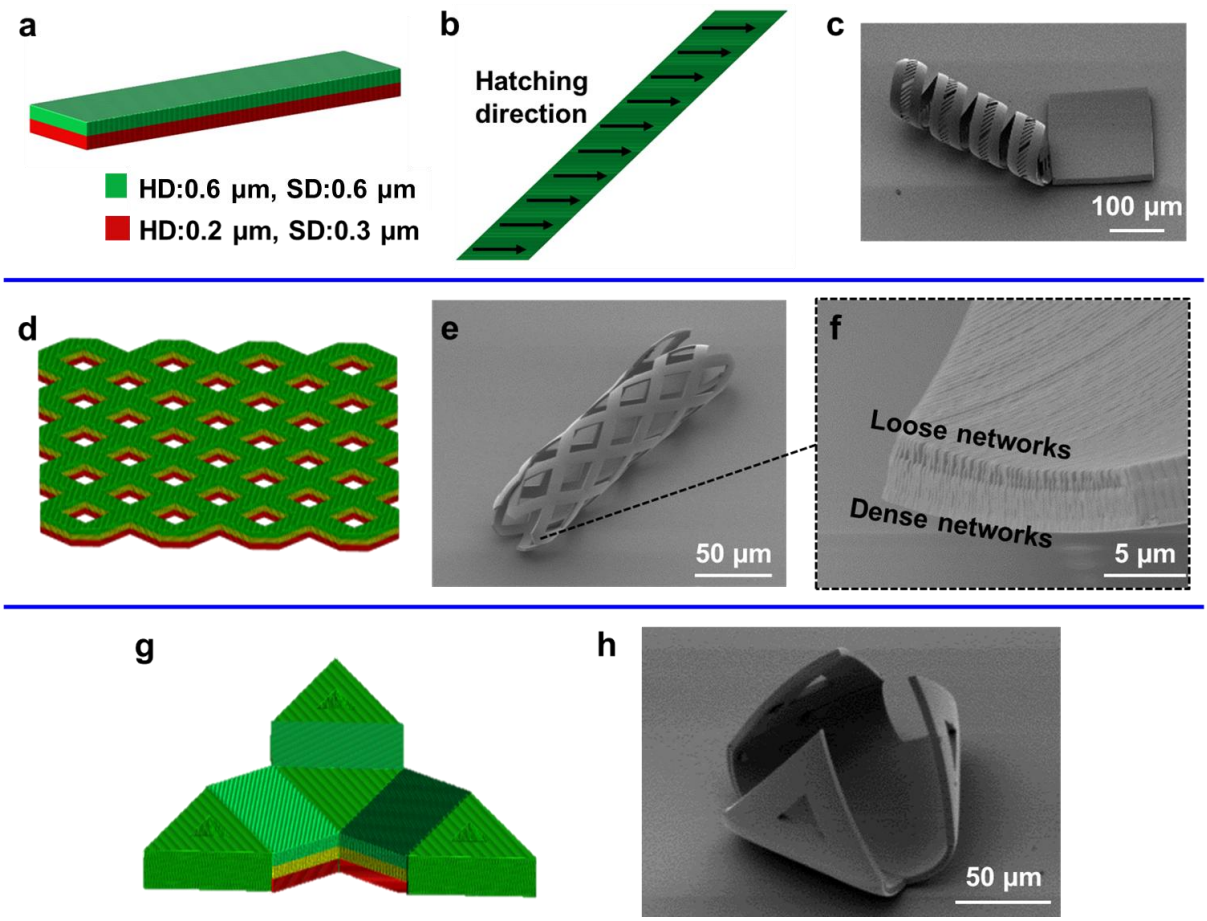

Figure S13. Flexible control of the 2D-3D transformation to construct various 3D micro-objects. a) Tilted-view and **b**) Top-view of the 2D design with the specific parameters for printing a microcoil. The laser power and scan speed used were 20 mW and 10 mm/s, respectively. **c**) SEM image of a typical microcoil structure. **d**) 2D unfolded pattern for a microstent. **e**, **f**) SEM images of the microstent after 2D-3D transformation. **g**) 2D design of a micro-origami structure. **h**) SEM image of the micro-origami structure after 2D-3D transformation.

In addition to the printing parameters (i.e., LP, SS, HD, and SD), the specific designs of the 2D patterns can also be used for controlling the stress fields and, thus, controlling the 2D-3D transformations. For example, we have designed a 2D pattern composed of multiple hexagon cells, as shown in **Figure S14**a.

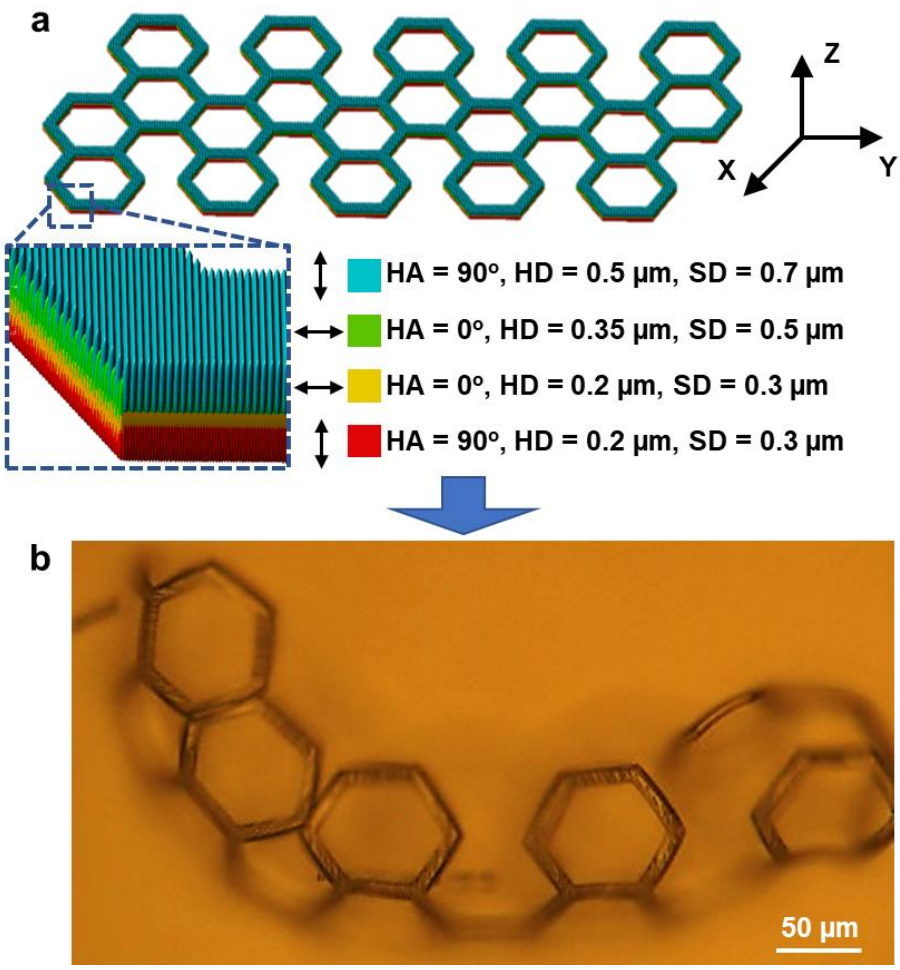

Figure S14. Constructing 3D curved truss structures via the 2D-3D transformation. a) 2D design for a typical truss structure. **b**) An optical micrograph of the truss structure after 2D-3D transformation.

Similar to the 2D films discussed above, DoC gradient can be introduced into each cell. Besides, the space within and among the hexagon cells provides more tunability on the structural transformation. The DoC gradient within each cell together with the topographic arrangement of the cells enabled the transformation of the 2D flat pattern to a 3D curved truss structure, as shown in **Figure S14**b. Since the flexibility of TPP permits the printing of arbitrary 2D patterns, various 3D truss structures can be printed and transformed.

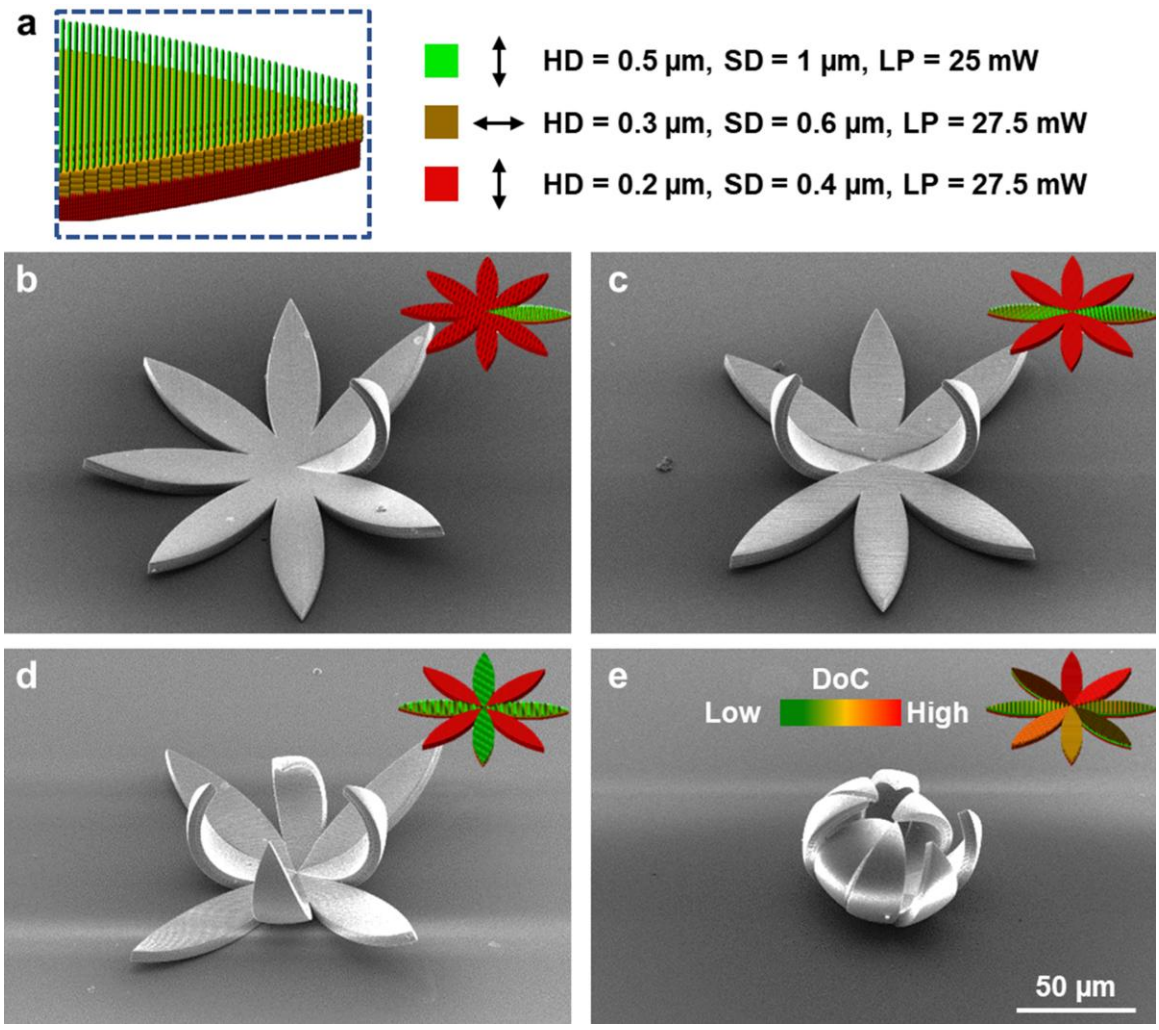

Figure S15. Controllable 2D-3D transformation by creating DoC gradients at different portions of TPP films. a) Specific parameters used for printing the petals bent in **b-d**. DoC gradients were created in one, two, and four petals in **b**, **c**, and **d**, respectively. **e**) DoC gradients of different levels were introduced in different petals to reach different bending curvatures. Insets are the 2D designs for introducing different DoC gradients.

To make the 2D-3D transformation applicable to constructing arbitrary 3D micro-objects, the capability of location- and shape- specific transformation is necessary. As shown in **Figure S15**, we have designed a flower-shaped 2D pattern composed of eight petals to demonstrate such a specific transformation process. It is confirmed that the 2D-3D transformation can be tailored to occur at a specific one or more petals (**Figure S15**b-d). Also, the eight petals can all be transformed to different degrees (**Figure S15**e).

2.5 Advantages of 2D-3D transformation over direct 3D printing

The stress-driven 2D-3D transformation approach developed in this research has substantial advantages over the conventional 3D printing. As demonstrated in **Figure S16**, direct 3D printing of objects with fragile features (e.g., long-flying, large-overhanging, suspending, or cantilever features) usually faces the challenges of structure collapse and mismatch of adjacent parts, causing failures of printing or unexpected surface roughness. Since the 2D-3D transformation uses only 2D in-plane printing, the collapse of fragile structures and mismatch between adjacent parts can be avoided,[9] with smoother surfaces and improved structural integrity achieved.

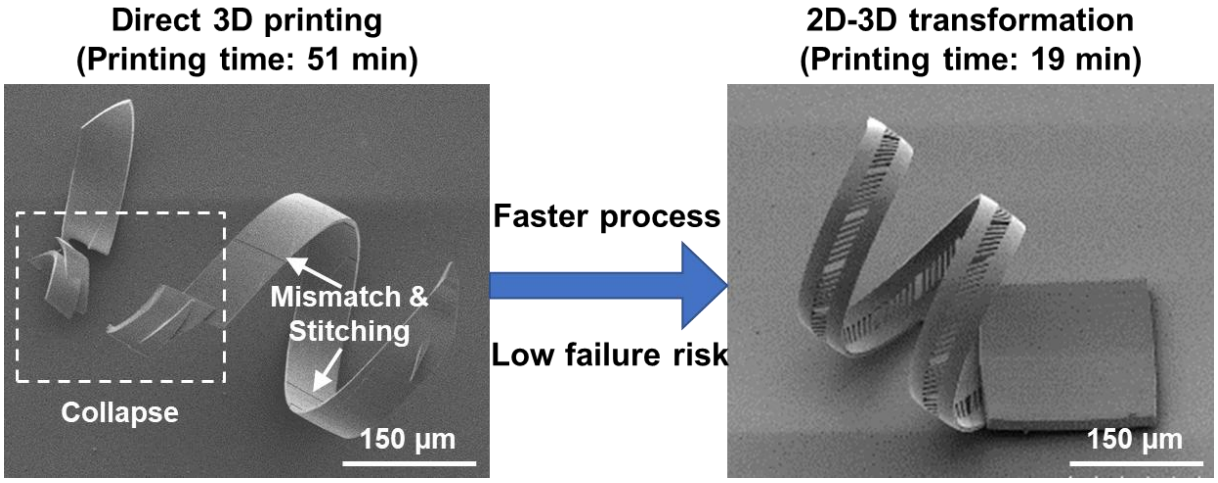

Figure S16. Comparison between the 2D-3D transformation and conventional 3D printing for fabricating the same structure.

The 2D-3D transformation can achieve higher production efficiencies. As shown in **Figures S16** and **S17**, the 2D-3D transformation approach requires only one fourth to one third of the time required by direct 3D printing to produce the same structures, regardless of their shapes and dimensions. In particular, more complex structures, e.g., microcoils with more pitches, require longer time to be fabricated through the direct 3D printing (**Figure S17**e-g). In contrast, microcoils with different pitches cost almost the same time to be fabricated through the 2D-3D transformation (**Figure S17**a-c), since they are formed from 2D patterns of the same dimensions.

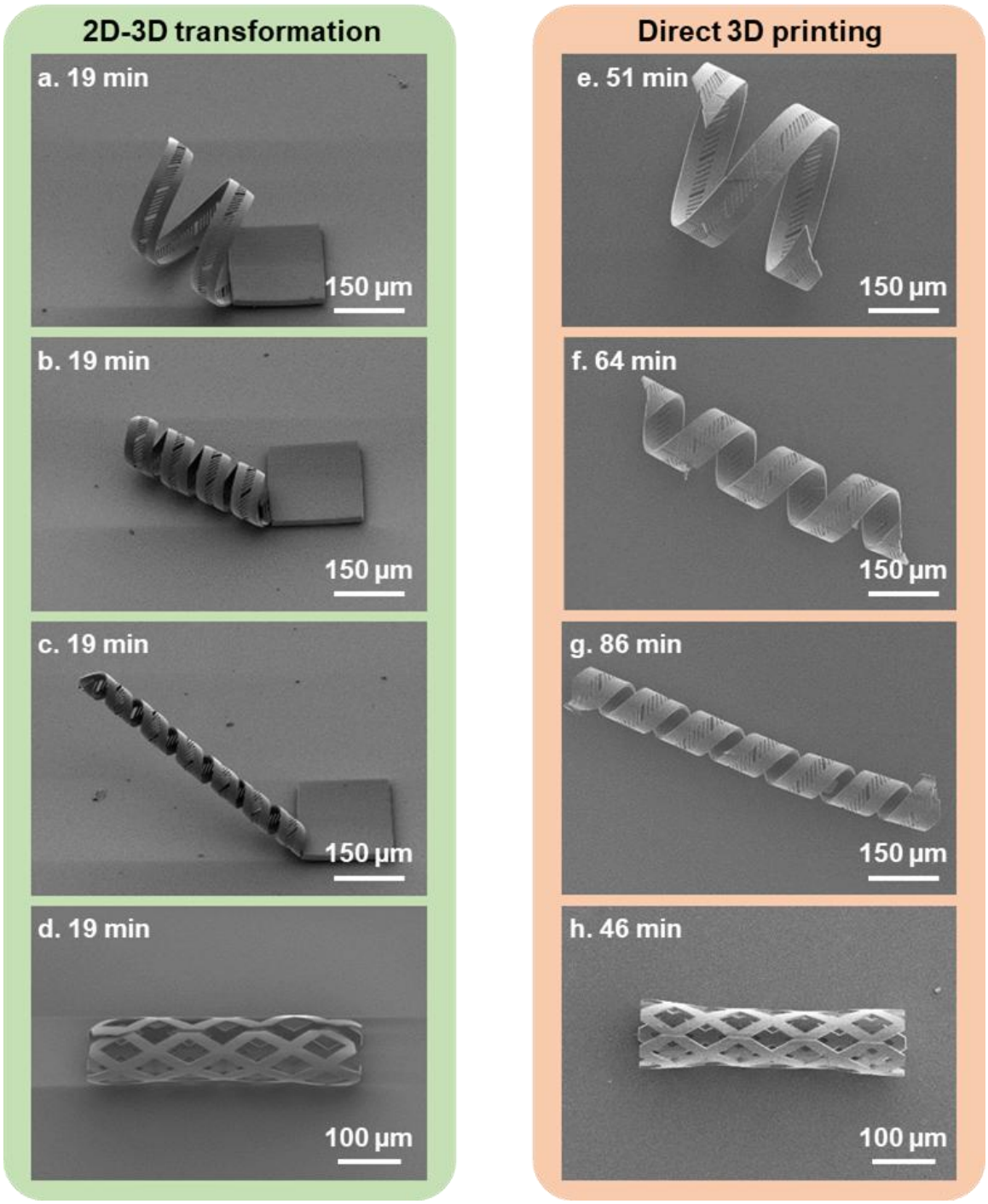

Figure S17. Comparison of printing times between the 2D-3D transformation and conventional 3D printing. The 2D-3D transformation requires much shorter printing times for producing the same structures.

Since no specific materials have been involved within the development of the approach, the 2D-3D transformation should also work for other polymer resins. In addition to the IP-Dip resin, two more representative polymer resins have been tested in our research. One is the IP-S resin

which is also purchased from the same vendor as the IP-Dip resin. The other one is the SU-8 resin which is a more commonly used photoresist in various fields. We succeeded in using both resins to fabricate the entire structures of the standing-flowers composed of multiple parts formed through different transformations (**Figure S18**), verifying the material independency of the 2D-3D transformation approach.

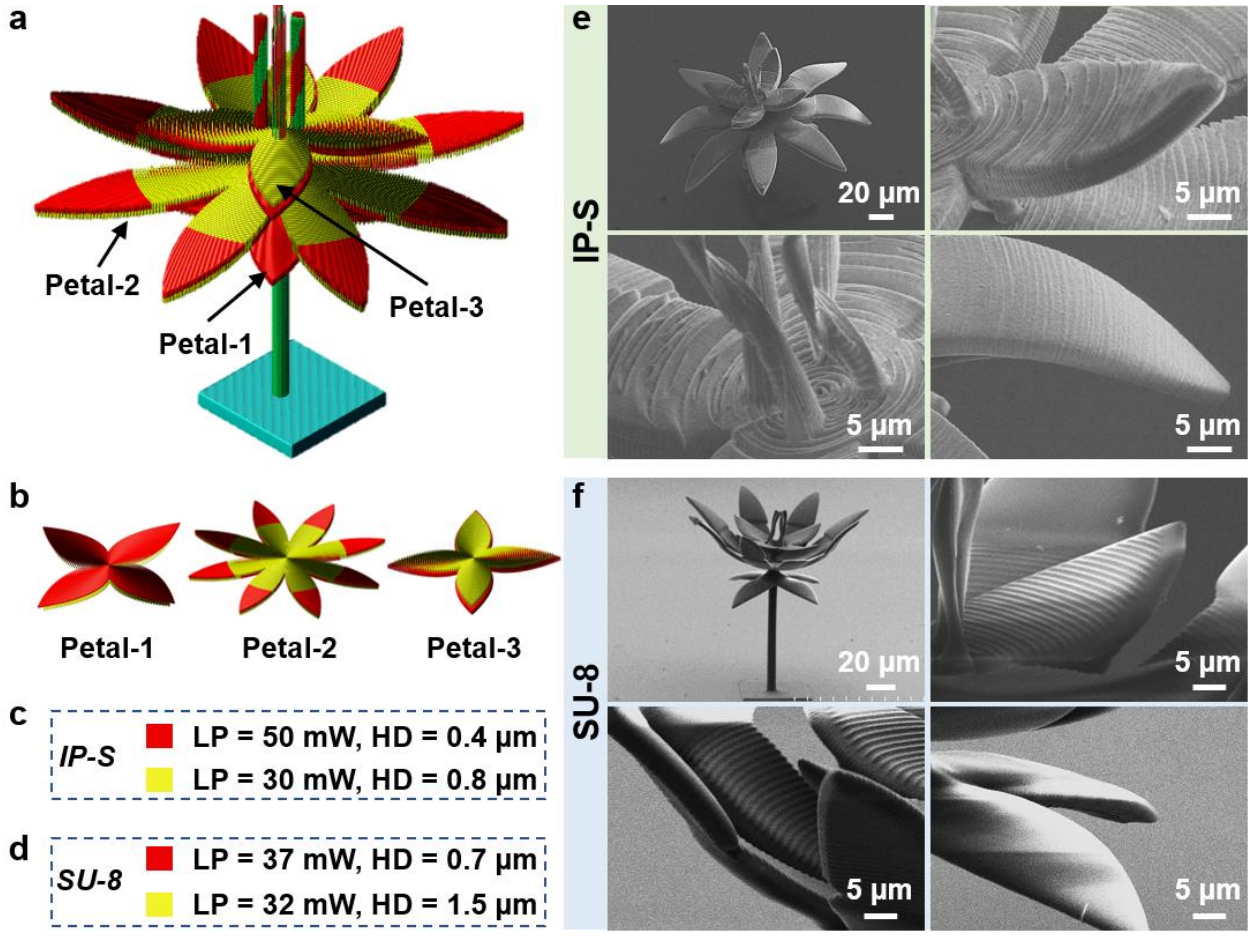

Figure S18. Fabrication of the entire structure of the standing-flower via 2D-3D transformations with the IP-S and SU-8 resins, respectively. a) Overview design of the entire structure of the standing-flower. **b**) Design of petals at three different heights. **c**) and **d**) Specific parameters for introducing DoC gradients with the IP-S and SU-8 resins, respectively. **e**) and **f**) SEM images for the entire standing-flower fabricated with the IP-S and SU-8 resins, respectively.

As a demonstration for practical applications of the gradient printing principle, we have tested the TPP fabrication of 3D curved lattice structures (**Figure S19**). Usually, such 3D lattice structures can only be fabricated via 3D printing due to their complex hollow and topological designs. However, the direct 3D printing fails in rendering the 3D lattice structures curved

orientations because they are susceptible to deformations (**Figure S19**c). To fabricate the 3D lattice structures with curved orientations using our approach, we set appropriate lateral DoC gradients during printing (**Figure S19**a). After development and structural transformation, the structure spontaneously bent to a bridge-shape geometry with all lattice features well maintained (**Figure S19**b).

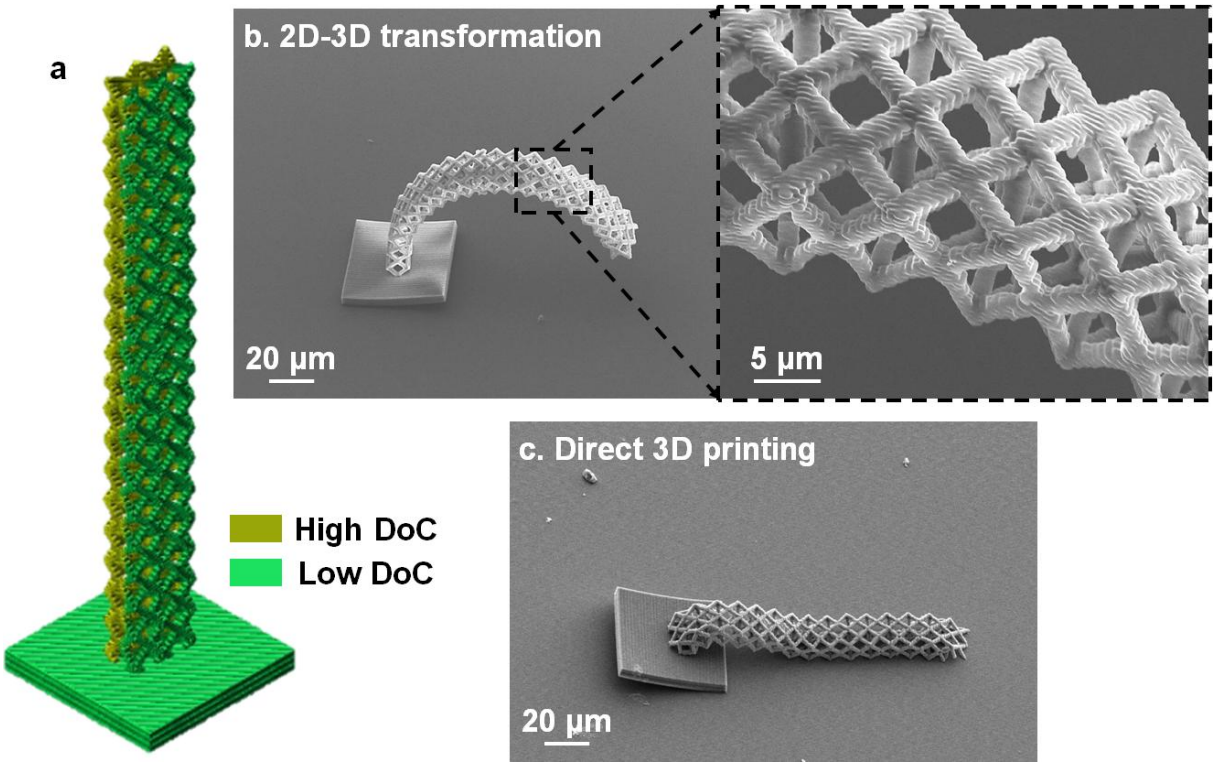

Figure S19. Fabrication of a 3D lattice structure with a curved orientation using the gradient printing principle. a) Design of the DoC gradients used for printing. **b**) Curved 3D lattice structure obtained through the gradient printing and transformation. **c**) Failure in realizing a curved lattice structure via direct 3D printing.

3. Supplemental Table

Specific TPP parameters for printing cubic blocks for bulk-shrinkage tests

Hatching distances	Controlling parameters	Parameter ranges	Other parameters
0.1 μm	Laser power	9.5-12 mW	SD = 0.2 μm SS = 10 mm/s
	Scan speed	40-90 mm/s	SD = 0.2 μm LP = 20 mW
0.2 μm	Laser power	11-15.5 mW	SD = 0.4 μm SS = 10 mm/s
	Scan speed	10-70 mm/s	SD = 0.4 μm LP = 20 mW
0.3 μm	Laser power	11-19 mW	SD = 0.6 μm SS = 10 mm/s
	Scan speed	5-55 mm/s	SD = 0.6 μm LP = 20 mW
0.4 μm	Laser power	14.75-21.25 mW	SD = 0.8 μm SS = 10 mm/s
	Scan speed	5-40 mm/s	SD = 0.8 μm LP = 20 mW
0.5 μm	Laser power	15.5-22 mW	SD = 1.0 μm SS = 10 mm/s
	Scan speed	5-25 mm/s	SD = 1.0 μm LP = 20 mW
0.6 μm	Laser power	17.75-23.25 mW	SD = 1.2 μm SS = 10 mm/s
	Scan speed	5-15 mm/s	SD = 1.2 μm LP = 20 mW

4. References

[1] T.-Y. Huang, H.-W. Huang, D.D. Jin, Q.Y. Chen, J.Y. Huang, L. Zhang, H.L. Duan, Sci. Adv. 6 (2020) eaav8219.

[2] M. Jamal, A.M. Zarafshar, D.H. Gracias, Nat. Commun. 2 (2011) 527.

[3] Y. Liu, J.H. Campbell, O. Stein, L. Jiang, J. Hund, Y. Lu, Nanomaterials 8 (2018).

[4] Y. Liu, W. Xiong, D.W. Li, Y. Lu, X. Huang, H. Liu, L.S. Fan, L. Jiang, J.-F. Silvain, Y.F. Lu, Int. J. Extreme Manuf. 1 (2019) 025001.

[5] S. Timoshenko, J. Opt. Soc. Am. 11 (1925) 233.

[6] X. Liu, M. Wei, Q. Wang, Y. Tian, J. Han, H. Gu, H. Ding, Q. Chen, K. Zhou, Z. Gu, Adv. Mater. 33 (2021) 2100332.